

## Research Article

# Preclinical Molecular PET-CT Imaging Targeting CDCP1 in Colorectal Cancer

**Tahleesa J. Cuda** <sup>1,2,3</sup> **Yaowu He**<sup>2</sup> **Thomas Kryza**<sup>2</sup> **Tashbib Khan**<sup>2</sup> **Brian W. Tse** <sup>4</sup> **Kamil A. Sokolowski**<sup>4</sup> **Cheng Liu**<sup>1,5,6</sup> **Nicholas Lyons**<sup>1,2</sup> **Madeline Gough**<sup>2,7</sup> **Cameron E. Snell**<sup>2,7</sup> **David K. Wyld**<sup>1,3</sup> **Stephen Rose**<sup>8</sup> **Andrew D. Riddell**<sup>9</sup> **Andrew R. L. Stevenson**<sup>1,3</sup> **Paul A. Thomas**<sup>1,3</sup> **David A. Clark**<sup>1,3</sup> **Simon Puttick**<sup>8</sup> **and John D. Hooper** <sup>2</sup>

<sup>1</sup>Faculty of Medicine, The University of Queensland, Brisbane, QLD, Australia

<sup>2</sup>Mater Research Institute The University of Queensland, Translational Research Institute, Woolloongabba, QLD, Australia

<sup>3</sup>Royal Brisbane and Women's Hospital, Metro North Hospital and Health Service, Brisbane, QLD, Australia

<sup>4</sup>Preclinical Imaging Core Facility, Translational Research Institute, Woolloongabba, QLD, Australia

<sup>5</sup>Envoi Specialist Pathologists, Herston, QLD, Australia

<sup>6</sup>QIMR Berghofer Medical Research Institute, Herston, QLD, Australia

<sup>7</sup>Mater Pathology, Mater Hospital Brisbane, Mater Health Services, Brisbane, QLD, Australia

<sup>8</sup>Commonwealth Scientific and Industrial Research Organisation, Herston, QLD, Australia

<sup>9</sup>Redcliffe Hospital, Metro North Hospital and Health Service, Brisbane, QLD, Australia

Correspondence should be addressed to John D. Hooper; [john.hooper@mater.uq.edu.au](mailto:john.hooper@mater.uq.edu.au)

Received 2 July 2021; Accepted 5 September 2021; Published 14 September 2021

Academic Editor: Luca Filippi

Copyright © 2021 Tahleesa J. Cuda et al. This is an open access article distributed under the Creative Commons Attribution License, which permits unrestricted use, distribution, and reproduction in any medium, provided the original work is properly cited.

Colorectal cancer (CRC) is the third most common malignancy in the world, with 22% of patients presenting with metastatic disease and a further 50% destined to develop metastasis. Molecular imaging uses antigen-specific ligands conjugated to radionuclides to detect and characterise primary cancer and metastases. Expression of the cell surface protein CDCP1 is increased in CRC, and here we sought to assess whether it is a suitable molecular imaging target for the detection of this cancer. CDCP1 expression was assessed in CRC cell lines and a patient-derived xenograft to identify models suitable for evaluation of radiolabelled 10D7, a CDCP1-targeted, high-affinity monoclonal antibody, for preclinical molecular imaging. Positron emission tomography-computed tomography was used to compare zirconium-89 (<sup>89</sup>Zr)-10D7 avidity to a nonspecific, isotype control <sup>89</sup>Zr-labelled IgGκ1 antibody. The specificity of CDCP1-avidity was further confirmed using CDCP1 silencing and blocking models. Our data indicate high avidity and specificity for <sup>89</sup>Zr-10D7 in CDCP1 expressing tumors at. Significantly higher levels than normal organs and blood, with greatest tumor avidity observed at late imaging time points. Furthermore, relatively high avidity is detected in high CDCP1 expressing tumors, with reduced avidity where CDCP1 expression was knocked down or blocked. The study supports CDCP1 as a molecular imaging target for CRC in preclinical PET-CT models using the radioligand <sup>89</sup>Zr-10D7.

## 1. Introduction

Colorectal cancer (CRC) is the third most common malignancy and the fourth leading cause of cancer-related death in the world [1]. Metastatic disease is the major cause of death with liver and lung the most common sites of

metastasis in 50–60% and 10–30% of CRC patients, respectively [2–5]. Staging and assessment of treatment response are aided by imaging using contrast-enhanced chest, abdominal and pelvic computed tomography (CT) with or without magnetic resonance (MR) and 2-deoxy-2-[F-18] fluorogluucose (FDG) positron emission tomography (PET)-

CT for improved anatomical localisation, lesion differentiation, and detection of small lesions [4, 6, 7].

Cancer diagnosis, risk stratification, therapy prognostication, and assessment of treatment efficacy can be improved by additional imaging approaches that noninvasively characterise and measure biological processes *in vivo* at the molecular level [8]. Molecular imaging integrates 2D or 3D imaging with cumulative quantification of cellular events using a variety of protocols including nuclear medicine radioligand imaging, MR imaging, MR spectroscopy, optical imaging, and ultrasound [9]. Radioligand molecular imaging employs ligands that incorporate a radionuclide conjugated to a peptide or antibody component that is specific for a protein enriched on the surface of malignant cells [10]. Systemically administered radioligands locate and bind to tumors and emit a radioactive signal to allow real-time detection using nuclear imaging modalities, such as PET, enabling determination of a range of clinically important parameters such as antigen biodistribution, anatomical location, pharmacokinetics, response to therapy, dose thresholds for malignant lesions, and off-target dosimetry [10–18]. As such, radioligand molecular imaging is a valuable tool for disease staging and guiding treatment decision making [2, 19, 20]. When combined with CT or MRI, both cellular and morphological features are acquired simultaneously [13].

An effective target protein for radioligand molecular imaging is expressed on the surface of tumor cells to be accessible to systemically delivered radioligands. To attain a high tumor-to-normal tissue ratio, candidate proteins should have homogeneous tumor expression with limited expression in normal tissue [17, 21]. Complement C1r/C1s, Uegf, Bmp1 domain-containing protein-1 (CDCP1) is a type I membrane-spanning glycoprotein with a 636 amino acid extracellular region, 20 amino acid transmembrane region, and 150 amino acid cytoplasmic domain [22, 23]. It is also known as subtractive immunisation M<sup>+</sup> HEP3-associated 135 kDa protein (SIMA135), Transmembrane and Associated with Src Kinases (TRASK), and cluster of differentiation 318 (CD318) [22, 23]. CDCP1 is expressed as a full-length 135 kDa protein and can also undergo proteolytic cleavage generating a 70 kDa membrane-spanning carboxyl-terminal fragment and a 65 kDa aminoterminal fragment that is either shed from the cell surface or remains bound to CDCP1 on the plasma membrane [24]. Previous studies have demonstrated the utility of mouse monoclonal 10D7 antibody that binds to the CDCP1 amino terminal, for delivery of Zirconium-89 (<sup>89</sup>Zr) for PET-CT-based detection, and cytotoxins for treatment of preclinical models of ovarian [25] and pancreatic [24] cancer. In CRC, elevated CDCP1 correlates with poorer patient outcome [3, 26]. Analysis of CDCP1 mRNA in a CRC cohort of 101 patients indicated that elevated levels correlate significantly with advanced stage, node metastasis, and diminished recurrence-free and overall survival [26]. Similarly, immunohistochemical analysis of 128 CRCs, including 38 cases without metastasis on presentation, 51 with liver metastasis, 35 with lung metastasis, and four with both liver and lung metastasis,

elevated CDCP1 correlated significantly with tumor size, grade and stage, and decreased lung metastasis free survival [3].

The present study aimed to investigate CDCP1 as a potential radioligand molecular imaging target for PET-CT detection of CRC in cell line xenograft and patient-derived mouse models using <sup>89</sup>Zr-labelled 10D7. The specificity of <sup>89</sup>Zr-10D7 for CDCP1 expressing CRC is explored using unlabelled 10D7 to compete for antibody binding sites and via silencing of CDCP1 expression to reduce the number of antibody binding sites.

## 2. Materials and Methods

**2.1. Cell Lines and Culture Conditions.** Human CRC HCT116, HT29 and SW480, prostate cancer PC3, and ovarian cancer OVMZ6 cell lines were obtained from ATCC (Manassas, VA). PC3 cell lines were maintained in RPMI 1640. CRC HCT116, HT29 and SW480, and ovarian cancer OVMZ6 cell lines were maintained in Dulbecco's Modified Eagle's Medium Media (Thermo Fisher Scientific, Seventeen Mile Rocks, Australia) containing 10% fetal calf serum (FCS) (Sigma-Aldrich, North Ryde, Australia), penicillin (100 units per mL), and streptomycin (100 units per mL) (Sigma-Aldrich) at 37°C in a humidified, 5% CO<sub>2</sub> atmosphere.

**2.2. Silencing of CDCP1 Expression.** CDCP1 expression was stably reduced in cells grown as spheroids isolated from a previously generated patient-derived xenograft (PDX), designated CRC13, as previously described [27, 28]. Cells from CRC13 spheroids mechanically dissociated in phosphate-buffered saline (PBS) containing EDTA (0.48 mM) were stably infected with a pLKO.1 lentiviral CDCP1 targeting shRNA (target sequence: GCTCATAA-GAGCATCGGTTTA; Open Biosystems, Millennium Science, Surrey Hills, Australia), or as a control, a non-targeting (control) shRNA (Addgene, Watertown, MA, USA) construct. Stably infected cells were grown as spheroids and selected in media containing puromycin (2 µg/ml) generating cells designated CRC13-shScr and CRC13-shCDCP1 which were propagated as subcutaneous tumors in mice as described below.

**2.3. Western Blot Analysis.** Whole cell lysates were collected in RIPA buffer (Sigma-Aldrich) containing 1x complete protease inhibitor cocktail (Roche, Castle Hill, NSW, Australia), 10 mM sodium fluoride, and 2 mM sodium vanadate. Lysates were used in western blot analysis as previously described [29] with rabbit anti-CDCP1 carboxyl-terminal antibody #4115 (dilution 1:2,000; Cell Signaling Technology, Genesearch, Arundel, Australia).

**2.4. Flow Cytometry.** At 50% confluence, adherent cells were nonenzymatically detached in PBS/EDTA (0.48 mM) and counted. Cells ( $2.5 \times 10^5$ ) were washed twice in PBS, blocked in PBS containing 2% FCS for 30 minutes, and stained with mouse anti-CDCP1 aminoterminal antibody 10D7 for 1

hour at 4°C [25]. Cells were then washed twice in PBS containing 2% FCS for 30 minutes at 4°C before incubation with an Alexa Fluor 488-conjugated goat anti-mouse secondary antibody at 4°C for 30 minutes (Thermo Fisher Scientific). Cells were washed in PBS twice more, then events (20,000/condition) were recorded and analysed using a FACs Fortessa flow cytometer.

**2.5. Subcutaneous Mouse Xenograft Models.** Experiments involving mice were approved by the University of Queensland Animal Ethics Committee (approval 112/17). Mice were housed in a pathogen-free environment with food and water provided ad libitum. Eight-week-old male NOD Cg-Prkdc<sup>scid</sup>IL2rg<sup>tm1Wjl</sup>/SzJ (NSG) mice (The Jackson Laboratory, Bar Harbor, ME) were injected subcutaneously with HCT116 cells ( $1 \times 10^6$ ) or spheroids of CRC13, CRC13-shScr or CRC-shCDCP1 cells (0.1 g/mouse of pelleted cell slurry in PBS suspension). Tumors were grown for three weeks prior to the commencement of radioligand molecular imaging experiments.

**2.6. Radiochemistry.** Conjugation of 1-(4-isothiocyanatophenyl)-3-[6,17-dihydroxy-7,10,18,21-tetraoxo-27-(N-acetylhydroxylamino)-6,11,17,22-tetraazaheptaicosine] thiourea (DFO-NCS) to 10D7 was performed as previously described [30]. Briefly, DFO-NCS (70 µg; ~93 nM) dissolved in dimethyl sulfoxide (5 µL) was reacted with 10D7 or isotype matched control IgGκ1 (1.5 mg; 10 nM) in 0.1 M Na<sub>2</sub>CO<sub>3</sub> (0.5 mL) for one hour at 37°C and pH 8.8–9.0. The reaction mixture was filtered by size exclusion chromatography using an AKTA Prime Plus (GE Life Sciences) fitted with a 5 mL HiTrap desalting column running a mobile phase of 0.1 M PBS at 0.5 mL/min. Radio labelling of DFO conjugated antibodies with <sup>89</sup>Zr was performed in accordance with published methods [30]. The pH of <sup>89</sup>Zr-oxalate (Perkin Elmer, Rowville, Australia) was adjusted to pH 7.0 using aliquots of 1M Na<sub>2</sub>CO<sub>3</sub> and buffered to pH 7.5 by 1:1 dilution in 0.5M HEPES. DFO-10D7 and DFO-IgGκ1 (1 mg) in 400 µL 0.5 M HEPES (pH 7.5) was mixed with 60MBq <sup>89</sup>Zr solution and incubated at 25°C for 60 minutes with mild agitation. Purification was then performed using a 7 kDa MWCO Zeba desalting column (Thermo Fisher Scientific) equilibrated with 0.1 M PBS (pH 7.2), yielding ~49MBq of <sup>89</sup>Zr-DFO-10D7 and <sup>89</sup>Zr-DFO-IgGκ1 in 0.5 mL (radiochemical yield 81%; concentration 98MBq/mL and 49MBq/mg). Thin-layer chromatography confirmed radiochemical purity >95% [30].

**2.7. Radioligand Biodistribution Analysis.** Mice ( $n=4$  per group) were anaesthetised with isoflurane and injected intravenously (i.v.) via lateral tail vein. For experiments using HCT116, mice were injected with one of the following regimes: (1) <sup>89</sup>Zr-10D7 (<sup>89</sup>Zr 1.4 MBq; 23 µg 10D7), (2) unlabelled 10D7 (1 mg) [31] after 60 minutes followed by <sup>89</sup>Zr-10D7 (<sup>89</sup>Zr 1.4 MBq; 23 µg 10D7), or (3) <sup>89</sup>Zr-IgG1κ (<sup>89</sup>Zr 1.4 MBq; 23 µg IgG1κ). Radioligand dosing was based on recent published data with increased dose provision to

lower CDCP1 tumor types [24]. For experiments using CRC13, <sup>89</sup>Zr-10D7 (<sup>89</sup>Zr 2 MBq; 33 µg 10D7), unlabelled 10D7 (1 mg) [31], followed after 60 minutes by <sup>89</sup>Zr-10D7 (<sup>89</sup>Zr 2 MBq; 33 µg 10D7) or <sup>89</sup>Zr-IgG1κ (<sup>89</sup>Zr 2 MBq; 33 µg IgG1κ). PET-CT imaging was performed at 1, 24, 48, 72, and 144 hours following radioligand administration using an Inveon PET-CT system (Siemens, Munich, Germany). Thirty-minute PET image acquisition was performed. CT imaging (10 minute acquisition) was performed for anatomical registration and attenuation correction (80 kV, 500 µA, 230 ms exposure time, 360° rotation with 180 rotation steps, binning factor of 4, low magnification position—producing an effective pixel size of 106 µm). CT images were reconstructed using the Feldkamp algorithm. PET images were reconstructed using an ordered subset expectation maximisation (OSEM2D) algorithm with CT attenuation correction. A conversion factor obtained from a cylindrical phantom filled with a known activity of <sup>89</sup>Zr was used to convert PET activity per voxel to becquerel (Bq)/cubic centimetre (cc). Image reconstruction and data analysis were performed using the Inveon Research Workspace (Siemens). *In vivo* tissue radioactivity was analysed at each time point within regions of interest (ROI) recorded as the percent of injected dose per unit volume (cubic centimetre) of tissue (%ID/cc). During measurement of each tumor deposit or organ, careful segmentation was performed only inclusive of the ROI. *Ex vivo* biodistribution of radioligand signal was performed after the 144-hour imaging time point. Mice were euthanised by CO<sub>2</sub> asphyxiation and a blood sample obtained by heart puncture. Tissues (tumor, heart, lungs, liver, kidneys, femur, muscle, tail, blood, and testes) were harvested and weighed. Radioactivity of ROIs was measured in a Wizard 2480 Automatic Gamma Counter (PerkinElmer) as the percent of the injected dose per unit weight (*g*) of tissue (%ID/*g*) calculated was corrected for decay and detector efficiency.

**2.8. Immunohistochemical Analysis.** Tumors were fixed in 10% neutral buffered formalin (Sigma-Aldrich) and then embedded in paraffin. Deparaffinised and rehydrated sections (5 µm) were stained with rabbit anti-CDCP1 carboxyl-terminal antibody #4115 (1:100) and haematoxylin and eosin (H&E) as previously described with signal developed using immunoperoxidase with DAB (DakoCytomation, Glostrup, Hovedstaden, Denmark) as the chromogenic substrate [29]. Sections were imaged with an Olympus DP26 camera and associated cellSens standard 1.7 imaging software (Olympus, Notting Hill, Australia). Staining was assessed by FRCPA anatomical pathologists (CL, CES).

**2.9. Statistical Analysis.** Statistical analyses were performed using GraphPad Prism 8 (GraphPad Software, San Diego, CA, USA). Statistical analyses of *in vivo* and *ex vivo* datasets were carried out individually, using two-tailed Student's *t*-test and two-way ANOVA analysis of variance. Values represent the mean ± standard deviation (SD). A value of  $p < 0.05$  was considered statistically significant. This paper was written in accordance with the ARRIVE guidelines [32].

### 3. Results

**3.1. Cell-Based and Mouse Xenograft Assays Identify HCT116 Cells as Suitable for Assessment of CDCP1-Directed Radioligand Molecular Imaging for CRC.** To identify a cell line suitable for CDCP1-targeted radioligand molecular imaging, flow cytometry assessing cell surface expression of CDCP1 was performed on the three CRC lines HT29, SW480, and HCT116, with ovarian cancer OVMZ6 cells used as a negative control and prostate cancer PC3 cells as a positive control [25,33]. As shown in Figure 1(a), cell surface levels of CDCP1 were the highest on HCT116 and SW480 cells, comparable to levels on prostate cancer PC3 cells, while levels were at least 50% lower on HT29 CRC cells. Western blot analysis of cell lysates indicated that CDCP1 is predominantly expressed by HCT116 cells as the full-length 135 kDa protein with only low levels of the 70 kDa carboxyl-terminal fragment generated by proteolysis (Figure 1(b)). High levels of primarily full-length CDCP1 retained on the plasma membrane should act as a suitable candidate for radioligand molecular imaging of HCT116 cell xenografts in mice.

**3.2. CDCP1-Targeted Molecular PET-CT Imaging Detects a CRC Cell Line Xenograft.** HCT116 cells grown as subcutaneous tumors in mice were employed to assess the ability of CDCP1-targeted molecular imaging to detect CRC *in vivo*. As summarized in Figure 2(a), after three weeks of HCT116 cell growth as xenografts, mice were injected i.v. with  $^{89}\text{Zr}$ -10D7, unlabelled 10D7 followed by  $^{89}\text{Zr}$ -10D7 after 60 minutes, or control  $^{89}\text{Zr}$ -IgG1 $\kappa$ , and PET-CT imaging was performed at 1, 24, 48, 72, and 144 hours later. Histological analysis of representative untreated subcutaneous HCT116 tumors revealed that xenografts display adenocarcinoma histological features (Figure 2(b) left) and CDCP1 expression which is located predominantly on the surface of malignant cells (Figure 2(b) right). These data confirm that HCT116 cell xenografts are suitable for assessment of CDCP1-directed molecular imaging of CRC *in vivo*.

*In vivo* PET analysis indicated that  $^{89}\text{Zr}$ -10D7 signal increased up to 72 hours then plateaued (Figures 2(c) and 2(d); statistical analysis in Table S1). It revealed that accumulation of  $^{89}\text{Zr}$ -10D7 in tumors ( $7.1 \pm 1.4\%$ ID/cc at 144 hours) was largely ablated by competition with unlabelled 10D7 ( $2.8 \pm 0.7\%$ ID/cc at 144 hours), while mice injected with control  $^{89}\text{Zr}$ -IgG1 $\kappa$  had negligible tumor avidity ( $0.8 \pm 0.1\%$ ID/cc at 144 hours). This analysis also demonstrated that in contrast to increasing  $^{89}\text{Zr}$ -10D7 signal in tumor up to 72 hours, off-tumor  $^{89}\text{Zr}$  signal in heart, lungs, and liver rapidly decreased in the first 24 hours and then plateaued in all groups of mice (Figure 2(d)).

At the end of the assay, quantitative radiometric gamma counter analysis was performed to further examine tumor and off-tumor radioactivity. The data are provided in Table S2, and statistically significant differences are shown in Table S3. The results demonstrate that endpoint radioactivity in tumors was 11.2 fold higher in mice administered  $^{89}\text{Zr}$ -

10D7 than  $^{89}\text{Zr}$ -IgG1 $\kappa$  (Figure 2(e); Table S2) confirming the CDCP1-specific binding and uptake apparent from the PET analysis. The specificity of 10D7 for CDCP1 expressing CRC cells *in vivo* was further confirmed by results showing that signal from xenograft tumors was 78% lower in mice coadministered unlabelled 10D7 and  $^{89}\text{Zr}$ -10D7 compared with mice administered only  $^{89}\text{Zr}$ -10D7 (Figure 2(e); Table S1).

Examination of off-tumor signal by *ex vivo* radiometric gamma counter analysis activity demonstrated the significantly higher hepatic activity of  $^{89}\text{Zr}$ -IgG1 $\kappa$  in comparison to  $^{89}\text{Zr}$ -10D7 coadministered with unlabelled 10D7, followed by  $^{89}\text{Zr}$ -10D7. It also revealed relatively lower blood, heart, lung, and renal activity of  $^{89}\text{Zr}$ -IgG1 $\kappa$  compared to  $^{89}\text{Zr}$ -10D7 coadministered with unlabelled 10D7 followed by  $^{89}\text{Zr}$ -10D7 (Figure 2(e)). These findings may be a consequence of reduced specific binding of  $^{89}\text{Zr}$ -IgG1 $\kappa$  resulting in increased hepatic uptake and catabolism as a mononuclear phagocyte system-containing organ [34–38]. Furthermore, high femoral activity was also identified in mice that received  $^{89}\text{Zr}$ -IgG1 $\kappa$  (Figure 2(e)). This finding further supports this hypothesis of increased  $^{89}\text{Zr}$ -IgG1 $\kappa$  hepatic catabolism with unbound  $^{89}\text{Zr}$  accumulating within unfused skeletal epiphyses of the skeletally immature mice used in these experiments, a known  $^{89}\text{Zr}$  phenomenon [39, 40]. High blood activity was detected in mice that received unlabelled 10D7 combined with  $^{89}\text{Zr}$ -10D7 ( $7.5 \pm 0.8\%$ ID/g) compared to  $^{89}\text{Zr}$ -10D7 and  $^{89}\text{Zr}$ -IgG1 $\kappa$  ( $5.0 \pm 0.6\%$ ID/g and  $0.5 \pm 0.0\%$ ID/g, respectively). We speculate that unlabelled 10D7 hepatic uptake and catabolism delayed the degradation of  $^{89}\text{Zr}$ -10D7, resulting in greater free circulating activity within the blood at 144 hours. Statistically significant differences in *ex vivo* activity are provided in Table S3.

**3.3. CDCP1-Targeted Molecular PET-CT Imaging Detects a CRC PDX.** To assess the effectiveness of a CDCP1-targeted agent against a more disease relevant model, PET-CT imaging was performed on PDX CRC13 [28]. This patient-derived model retains the features of the original primary colon cancer displaying histology of a poorly differentiated adenocarcinoma (Figure 3(a) left) and prominent cell surface localisation of CDCP1 (Figure 3(a) right). After three weeks of CRC13 growth, PET-CT imaging of mice at 1, 24, 48, 72, and 144 hours after i.v. administration of radio-labelled antibodies indicated increasing accumulation of  $^{89}\text{Zr}$ -10D7 signal in subcutaneous flank tumors with negligible tumor signal from mice injected with control  $^{89}\text{Zr}$ -IgG1 $\kappa$  (Figure 3(b)). As was observed for the HCT116 cell xenograft model, both  $^{89}\text{Zr}$ -10D7 and  $^{89}\text{Zr}$ -IgG1 $\kappa$  accumulated in liver and the cardiopulmonary system with signal reducing significantly 24 hours after administration by *in vivo* PET analysis (Figure 3(c)). Quantitative analysis of signal from tumor, heart, lung, and liver indicated increasing  $^{89}\text{Zr}$ -10D7 tumor avidity over the time course and the highest avidity at the 144-hour time point ( $6.8 \pm 1.6\%$ ID/cc) whereas signal from heart, lung, and liver reduced during this time period (Figure 3(c)). These results were confirmed by quantitative *ex vivo* biodistribution analysis of  $^{89}\text{Zr}$ -10D7 and  $^{89}\text{Zr}$ -IgG1 $\kappa$

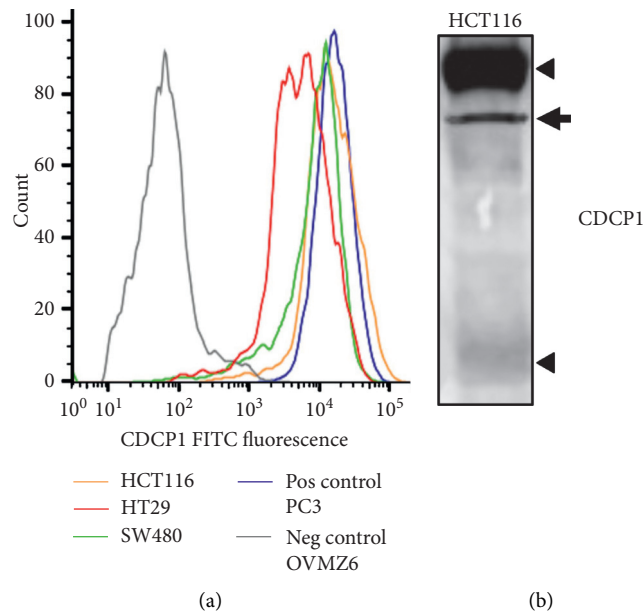


FIGURE 1: Cell-based and mouse xenograft assays identify HCT116 cells for assessment of CDCP1-directed radioligand molecular imaging for CRC. (a) Flow cytometry evaluation of cell surface CDCP1 expression on HCT116, SW480, and HT29 CRC cell lines, positive control prostate cancer PC3 cells, and negative control ovarian cancer OVMZ6 cells. Cells were stained with anti-CDCP1 antibody 10D7 then Alexa Fluor 488 tagged goat-anti-mouse secondary antibody. Cells stained only with the secondary antibody provided background signal. Signals were normalised to mode. (b) Western blot analysis for CDCP1 of lysates from HCT116 cells using anti-carboxyl terminal antibody 4115. Arrowheads indicate full-length 135 kDa and cleaved 70 kDa CDCP1. An incompletely N-glycosylated form of CDCP1 is indicated by the arrow.

in recovered tumors, organs, and blood. As shown in Figure 3(d), markedly higher activity was detected in tumors from mice administered  $^{89}\text{Zr}$ -10D7 ( $13.1 \pm 1.7\% \text{ID/g}$ ) compared to  $^{89}\text{Zr}$ -IgG1 $\kappa$  ( $4.9 \pm 0.8\% \text{ID/g}$ ). Radioactivity was approximately the same in lung, tail, and testes from these mice, and levels were higher in liver and femur of mice administered  $^{89}\text{Zr}$ -IgG1 $\kappa$ , while levels were marginally higher in heart, kidney, and muscle of mice administered  $^{89}\text{Zr}$ -10D7 (Figure 3(d) and Table S4). Surprisingly, signal was considerably higher in the blood of mice administered  $^{89}\text{Zr}$ -10D7 compared with  $^{89}\text{Zr}$ -IgG1 $\kappa$  (Figure 3(d) and Table S4) likely as a result of reduced nonspecific accumulation of  $^{89}\text{Zr}$ -10D7 in off-target tissues resulting in increased, free circulating  $^{89}\text{Zr}$ -10D7 compared to  $^{89}\text{Zr}$ -IgG1 $\kappa$ . Overall findings of this experiment correlate with those from the HCT116 CRC model presented earlier.

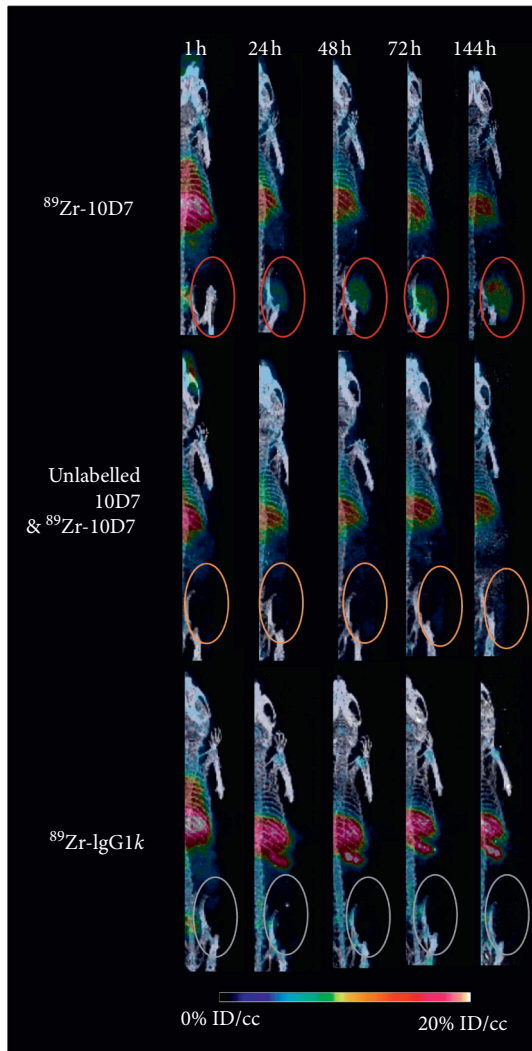
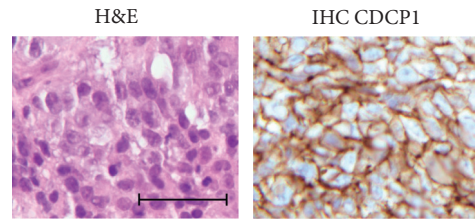
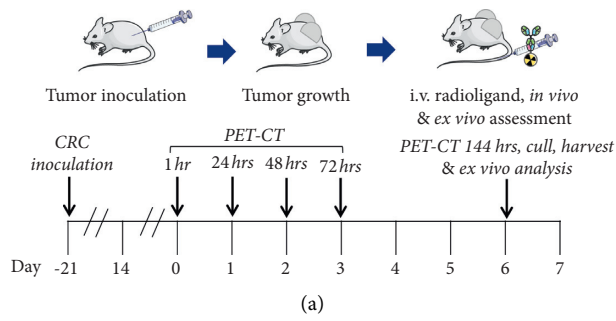
To examine the impact of reduced CDCP1 expression on  $^{89}\text{Zr}$ -10D7 tumor avidity, PET-CT imaging results were compared from CRC13 xenografts stably transduced with a lentivirus CDCP1 silencing construct (CRC13-shCDCP1) or a scramble control construct (CRC13-shScr). As shown in Figure 4(a), histochemical analyses indicated that CDCP1 expression was markedly reduced in CRC13-shCDCP1 compared to CRC13-shScr tumors (top) and the histology of xenografts was unaltered by reduced levels of this protein (bottom). Twice weekly measurement of xenograft volume indicated that tumor growth was unaffected by silencing of CDCP1. PET-CT imaging of mice administered  $^{89}\text{Zr}$ -10D7 indicated that after 24 hours, CRC13-shCDCP1 tumors (blue circle) with reduced levels of CDCP1 had significantly

lower avidity than control CRC13-shScr tumors (red circle) and the difference in avidity increased over time (Figure 4(b)). Quantitative imaging and radiometric analyses indicated that  $^{89}\text{Zr}$ -10D7 tumor avidity was reduced by about 40% in CRC13-shCDCP1 ( $6.5 \pm 1.0\% \text{ID/g}$ ) compared to CRC13-shScr ( $10.8 \pm 1.3\% \text{ID/g}$ ) tumors (Figures 4(c) and 4(d)). Although IHC analysis confirmed nearly 100% downregulation of CDCP1 expression in CRC13-shCDCP1 compared to CRC13-shScr tumors, tumor avidity varied by 40%.

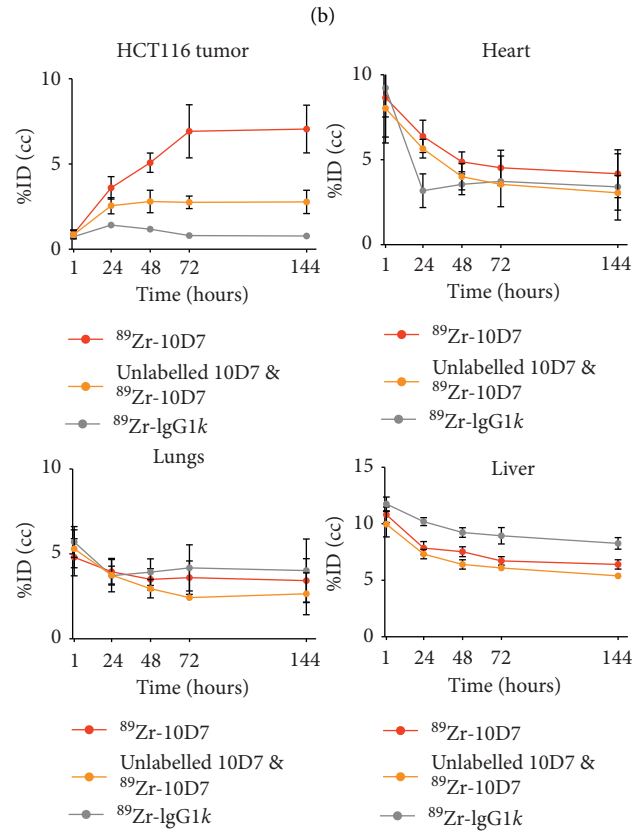
#### 4. Discussion

Using cell line xenograft and patient-derived models in mice, our data indicate that the radio-labelled antibody agent,  $^{89}\text{Zr}$ -10D7, directed against the receptor CDCP1, can be employed in PET-CT imaging to detect CRC *in vivo*. Combined with previous reports of elevated CDCP1 in CRC patient cohorts [3, 26], our results suggest that clinical implementation of a CDCP1-directed PET-CT imaging agent could have utility in CRC including for staging and assessment of treatment response as an aid to existing modalities of CT, MR, and FDG PET-CT imaging.

We have previously shown that antibody-based CDCP1 directed agents are effective for PET-CT imaging and treatment of preclinical models of ovarian [25] and pancreatic [24] cancer. The present study demonstrates the utility of a  $^{89}\text{Zr}$ -labelled CDCP1-directed agent (10D7) for CRC and also extends the ovarian and pancreatic cancer studies by demonstrating the selectivity of  $^{89}\text{Zr}$ -10D7 for

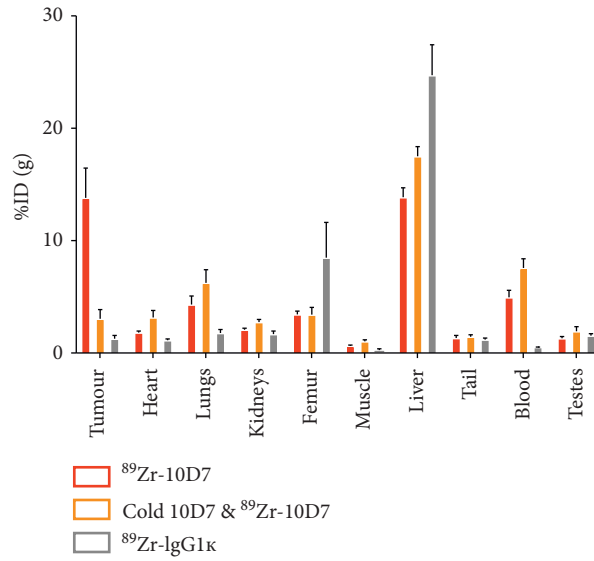


(c)



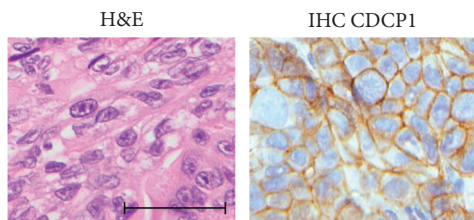
(d)

FIGURE 2: Continued.

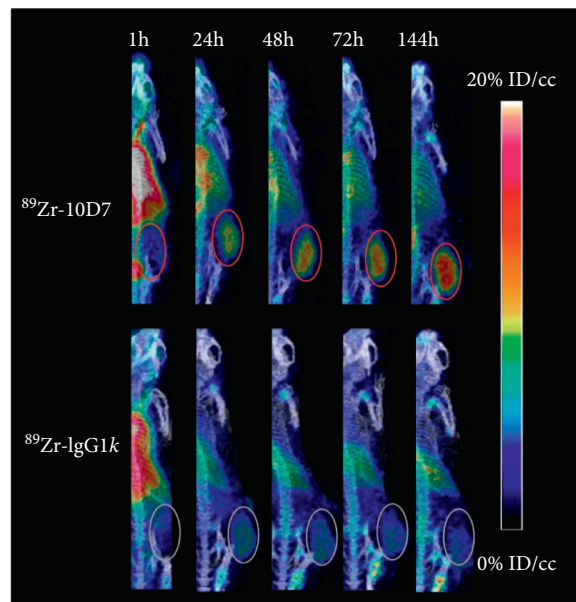


(e)

FIGURE 2: CDCP1 targeted molecular PET-CT imaging detects a CRC cell line xenograft. (a) Diagram of HCT116 cell inoculation followed by a period of tumor growth, radioligand administration PET-CT imaging. (b) Representative H&E staining (left) and anti-CDCP1 immunohistochemical staining (right) demonstrating strong plasma membrane staining of CDCP1 on malignant cells in subcutaneous HCT116 cell xenograft tumors in mice (magnification 40X; scale bar 50 μm). (c) Representative 3D PET-CT imaging reconstructions of mice bearing subcutaneous HCT116 cell xenografts administered i.v. <sup>89</sup>Zr-10D7, unlabelled 10D7 with <sup>89</sup>Zr-10D7, or <sup>89</sup>Zr-IgG1κ (1.4MBq) at 1, 24, 48, 72, and 144 hours after administration. (d) Graph of the time course of *in vivo* PET avidity of HCT116 cell xenograft tumor, heart, lungs, and liver at 1, 24, 48, 72, and 144 h after i.v. administration of <sup>89</sup>Zr-10D7, unlabelled 10D7 with <sup>89</sup>Zr-10D7, and <sup>89</sup>Zr-IgG1κ. Error bars are present for <sup>89</sup>Zr-IgG1κ but at the scale are too small to be apparent. (e) Graph of radioactivity of recovered tumors measured by *ex vivo* radiometric analysis and displayed as %ID/g. \*\*, *p* < 0.01.



(a)



(b)

FIGURE 3: Continued.

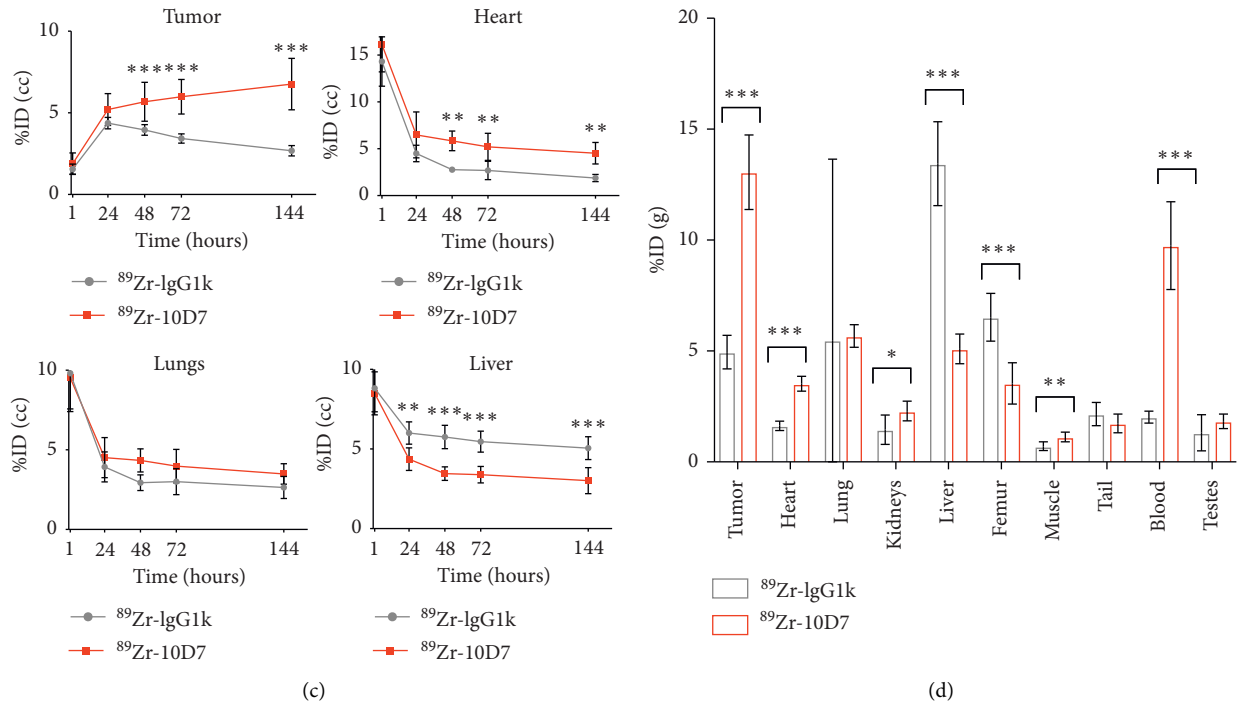


FIGURE 3: CDCP1-targeted molecular PET-CT imaging detects CDCP1-expressing patient-derived CRC13 model in mice. (a) Representative image of H&E stained (left) and anti-CDCP1 immunohistochemical staining (right) demonstrating moderate plasma membrane staining of CDCP1 on malignant cells in subcutaneous CRC13 xenograft tumors in mice (magnification 40X; scale bar  $50\ \mu\text{m}$ ). (b) Representative 3D PET-CT imaging reconstructions of mice bearing subcutaneous CRC13 tumors administered i.v.  $^{89}\text{Zr}$ -10D7 or  $^{89}\text{Zr}$ -IgG1 $\kappa$  (1MBq) at 1, 24, 48, 72, and 144 h after administration. (c) Graph of the time course of *in vivo* PET avidity of CRC13 tumors at 1, 24, 48, 72, and 144 h after i.v. administration of  $^{89}\text{Zr}$ -10D7 and  $^{89}\text{Zr}$ -IgG1 $\kappa$ . (d) Graph of radioactivity of recovered tumors, organs, and blood by *ex vivo* radiometric analysis and displayed as %ID/g. \*,  $p < 0.05$ ; \*\*,  $p < 0.01$ ; \*\*\*,  $p < 0.001$ .

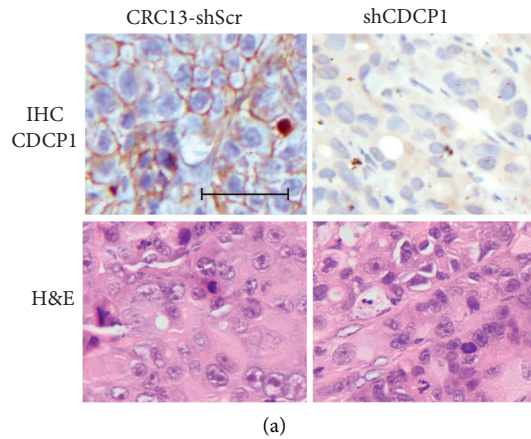


FIGURE 4: Continued.

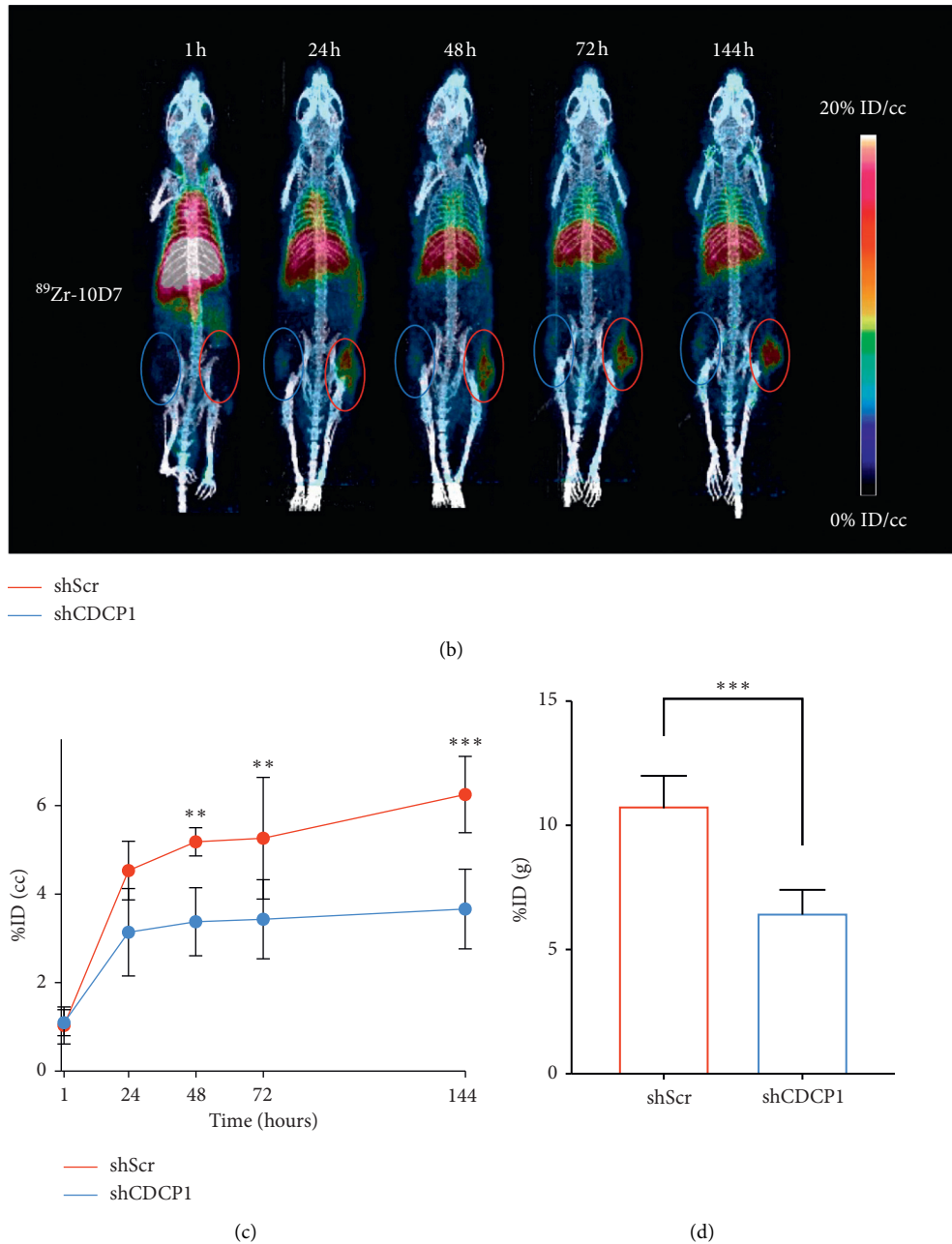


FIGURE 4: Reduced CDCP1 expression reduces avidity of CDCP1-targeting antibody 10D7 for patient-derived model CRC13 in mice. (a) Representative image of H&E stained (bottom) and anti-CDCP1 immunohistochemical staining (top) of subcutaneous CRC13-shScr (left) and CRC13-shCDCP1 (right) xenografts in mice. Anti-CDCP1 immunohistochemistry demonstrated markedly reduced expression of CDCP1 in CRC13-shCDCP1 tumors compared with CRC13-shScr tumors. H&E staining indicated that histology of xenografts was unaltered by reduced levels of CDCP1 (scale bar 50  $\mu$ m). (b) Representative 3D PET-CT reconstructions of mice bearing CRC13-shScr (red circle) and CRC13-shCDCP1 (blue circle) tumors at 1, 24, 48, 72, and 144 hours after  $^{89}\text{Zr}$ -10D7 administration (1MBq). (c) *In vivo* PET avidity of tumors at time points following  $^{89}\text{Zr}$ -10D7 administration displayed as %ID/cc. (d) Quantitative *ex vivo* biodistribution data determined by radiometric analysis of excised tumors at the end of the assay. \*,  $p < 0.05$ ; \*\*,  $p < 0.01$ ; \*\*\*,  $p < 0.001$ .

CDCP1 expressing tumors using unlabelled 10D7. The addition of high dose, unlabelled ligands is a recognized method to demonstrate *in vivo* target-specific blocking [41–43]. Our results indicate that unlabelled 10D7 competes with  $^{89}\text{Zr}$ -10D7 for CDCP1 binding sites, thereby reducing PET signal by ~60%, comparable to similar experimental design in existing publications [42, 44]. CRC13-shCDCP1

tumors had ~40% reduced tumor avidity compared to CRC13-shSrc tumors. Comparable reductions are seen with other published silencing models [45]. Additionally, the peak avidity of CRC13-shCDCP1 tumors administered  $^{89}\text{Zr}$ -10D7 and nontransfected CRC13 administered  $^{89}\text{Zr}$ -IgG1 $\kappa$  was comparable. Residual radioligand uptake from silenced and nonspecific ligand experiments is attributed to

nonspecific enhanced permeability (EPR) and retention effect [43], with exaggerated effects in most rapidly growing solid tumors [46] and *in vivo* small animal xenograft tumor models [47].

An underlying principle of radioligand molecular imaging is the provision of the lowest effective dose while maintaining diagnostically adequate spatial resolution [48]. The half-life of the chosen radionuclide must approximate that of the selected ligand [19].  $^{89}\text{Zr}$  has a long half-life of 78.4 hours, making it suitable for full-length antibodies, such as 10D7 [19, 39]. However, the prolonged activity of such radionuclides results in increased off-target exposure [49]. As experienced in the *in vivo* models in this study, late imaging time points following the administration of a radiolabelled antibody are required to detect peak tumor-to-background avidity, at the expense of increased radiation exposure [19]. Peak *in vivo*  $^{89}\text{Zr}$ -10D7 tumor-to-background signal was detected at 144 hours. Antibodies appeal as ligands because of high target specificity and affinity [50]. However, ligand serum half-life is dependent on size and structure [19, 39], with the relatively high molecular weight of ~150 kDa of full-length antibodies such as 10D7 [24] requiring several days to reach peak tumor-to-background signal ratio due to initial blood pool and slower perfusion times compared to smaller vectors [40, 50–52]. The delay in achieving adequate tumor-to-background signal after agent administration may negatively impact clinical implementation of an antibody-based CDCP1-directed PET imaging agent for CRC and other cancers.

Another factor impacting implementation of a  $^{89}\text{Zr}$ -labelled antibody against CDCP1 is *in vivo* radionuclide metabolism and dissociation which results in 5–10% of conjugated  $^{89}\text{Zr}$  dissociating within 48 hours after administration. This is a clinical issue because unbound  $^{89}\text{Zr}$  accumulates in radiosensitive bone and skeletal growth plates, reducing its diagnostic utility and increasing bone marrow radiation dose [39, 40]. Another issue is the phenomena of *in vivo* transmetallation or transchelation of  $^{89}\text{Zr}$  with metal complexing proteins such as transferrin and ceruloplasmin in the liver and kidneys which also increases off-tumor irradiation [49].

These issues may be addressed by employing smaller CDCP1-targeted ligands including antibody fragments or peptides. Reducing the molecular size of full-length antibodies by altering the Fc receptor-binding domain can accelerate peak tumor-to-background ratio and improve blood clearance, tumor retention, and PET avidity [15]. Antibody fragments and peptides are smaller ligands with lower molecular weights and reduced serum half-lives which can more easily perfuse tissue [20, 39]. Antibody fragments typically share the same high-affinity binding and specificity properties as full-length counterparts [50] and some peptides also exhibit similar binding affinities as full-length antibodies with the added advantage of rapid tissue penetration [50, 52]. Peptides can also be resistant to protease hydrolysis, increasing *in vivo* stability [52]. In addition, low molecular weight ligands such as peptides are suited for radionuclides with short half-lives including  $^{18}\text{F}$  (half-life 109.8 min) and  $^{68}\text{Ga}$  (half-life 67.6 min) [19, 39, 50]. Such radionuclides are favoured for

radioligand molecular imaging as imaging can be performed soon after administration in a clinically manageable time-frame with reduced effective dose and minimal residual radioactivity on patient discharge [53, 54].

## 5. Conclusions

In summary, the preclinical murine models in this paper support CDCP1 as a radioligand molecular imaging target for CRC. Quantitative analysis by flow cytometry and semiquantitative analysis by immunohistochemistry confirm CDCP1 expression in a range of CRC cell lines and a PDX. Statistically significant high tumor uptake of the radiolabelled antibody  $^{89}\text{Zr}$ -10D7 was found in two CDCP1-expressing CRC mouse models at late imaging time points with specificity indicated on protein silencing and epitope blocking models. The findings support further work to examine CDCP1 as a radioligand molecular imaging target for CRC.

## Data Availability

The data used to support the findings of this study are available from the corresponding author upon request.

## Conflicts of Interest

Yaowu He, Thomas Kryza, Simon Puttick, and John Hooper are inventors on a Patent Filing for 10D7-based CDCP1-targeted biomolecules.

## Acknowledgments

The authors acknowledge the Translational Research Institute for providing the core facilities that enabled this research, particularly the Biological Resources Facility, Microscopy Facility, and Preclinical Imaging Facility. This work was supported by grants from the Therapeutic Innovation Australia Pipeline Accelerator Scheme, the National Health and Medical Research Council of Australia (APP1121970), and Medical Research Future Fund (MRF1199422); by philanthropic support from the Mater Foundation to JDH; grants to TC, SR, PAT, and JDH from Brisbane Diamantina Health Partners, to SR and JDH from Tour de Cure (RSP-256-18/19), and to TC, ARLS, and JDH from the Colorectal Surgical Society ANZ Foundation; and by a higher degree scholarship from The University of Queensland Graduate School to Tashbib Khan. The Translational Research Institute is supported financially by the Queensland State Government and Australian Federal Government.

## Supplementary Materials

Table S1: two-way ANOVA of statistically significant *in vivo* PET avidity (%ID/cc) of HCT 116 tumors for imaging time points. Table S2: *ex vivo* radiometric gamma analysis activity (%ID/g mean  $\pm$  SD) of HCT116 tumors at 144 hours. Table S3: two-way ANOVA of statistically significant *ex vivo*

radiometric gamma analysis activity (%ID/g) of HCT116 tumors at 144 hours. Table S4: *ex vivo* radiometric gamma analysis activity (%ID/g mean  $\pm$  SD) of CRC13 at 144 hours. (Supplementary Materials)

## References

- [1] P. Favoriti, G. Carbone, M. Greco, F. Pirozzi, R. E. M. Pirozzi, and F. Corcione, "Worldwide burden of colorectal cancer: a review," *Updates in Surgery*, vol. 68, no. 1, pp. 7–11, 2016.
- [2] S. J. Clarke, C. S. Karapetis, P. Gibbs et al., "Overview of biomarkers in metastatic colorectal cancer: tumour, blood and patient-related factors," *Critical Reviews in Oncology*, vol. 85, no. 2, pp. 121–135, 2013.
- [3] W. Gao, L. Chen, Z. Ma et al., "Isolation and phenotypic characterization of colorectal cancer stem cells with organ-specific metastatic potential," *Gastroenterology*, vol. 145, no. 3, pp. 636–646, 2013.
- [4] H. Brenner, M. Kloor, and C. P. Pox, "Colorectal cancer," *The Lancet*, vol. 383, no. 9927, pp. 1490–1502, 2014.
- [5] K. Kitajima, M. Nakajo, H. Kaida et al., "Present and future roles of FDG-PET/CT imaging in the management of gastrointestinal cancer: an update," *Nagoya Journal of Medical Science*, vol. 79, pp. 527–543, 2017.
- [6] D. H. Lee and J. M. Lee, "Whole-body PET/MRI for colorectal cancer staging: is it the way forward?" *Journal of Magnetic Resonance Imaging*, vol. 45, no. 1, pp. 21–35, 2017.
- [7] M. C. Niekel, S. Bipat, and J. Stoker, "Diagnostic imaging of colorectal liver metastases with CT, MR imaging, FDG PET, and/or FDG PET/CT: a meta-analysis of prospective studies including patients who have not previously undergone treatment," *Radiology*, vol. 257, no. 3, pp. 674–684, 2010.
- [8] F. A. Jaffer and R. Weissleder, "Molecular imaging in the clinical arena," *Jama*, vol. 293, no. 7, pp. 855–862, 2005.
- [9] D. A. Mankoff, "A definition of radioligand molecular imaging," *Journal of Nuclear Medicine*, vol. 48, p. 18, 2007.
- [10] J. R. Lindner and J. Link, "Molecular imaging in drug discovery and development," *Circulation: Cardiovascular Imaging*, vol. 11, no. 2, Article ID e005355, 2018.
- [11] L. H. Mammatas, H. M. W. Verheul, N. H. Hendrikse, M. Yaqub, A. A. Lammertsma, and C. W. Menke-van der Houven van Oordt, "Molecular imaging of targeted therapies with positron emission tomography: the visualization of personalized cancer care," *Cellular Oncology*, vol. 38, no. 1, pp. 49–64, 2015.
- [12] R. Huang, M. Wang, Y. Zhu, P. Conti, and K. Chen, "Development of PET probes for cancer imaging," *Current Topics in Medicinal Chemistry*, vol. 15, no. 8, pp. 795–819, 2015.
- [13] A. Dimitrakopoulou-Strauss, "PET-based molecular imaging in personalized oncology: potential of the assessment of therapeutic outcome," *Future Oncology*, vol. 11, no. 7, pp. 1083–1091, 2015.
- [14] R. L. Wahl, J. M. Herman, and E. Ford, "The promise and pitfalls of positron emission tomography and single-photon emission computed tomography molecular imaging-guided radiation therapy," *Seminars in Radiation Oncology*, vol. 21, no. 2, pp. 88–100, 2011.
- [15] S. Kaur, G. Venktaraman, M. Jain, S. Senapati, P. K. Garg, and S. K. Batra, "Recent trends in antibody-based oncologic imaging," *Cancer Letters*, vol. 315, no. 2, pp. 97–111, 2012.
- [16] M. F. Fiordelisi, L. Auletta, L. Meomartino et al., "Preclinical molecular imaging for precision medicine in breast cancer mouse models," *Contrast Media and Molecular Imaging*, vol. 2019, Article ID 8946729, 15 pages, 2019.
- [17] P. M. Clark, V. A. Ebiana, L. Gosa, T. F. Cloughesy, and D. A. Nathanson, "Harnessing preclinical molecular imaging to inform advances in personalized cancer medicine," *Journal of Nuclear Medicine*, vol. 58, no. 5, pp. 689–696, 2017.
- [18] F. Man and T. Lammers, "Imaging nanomedicine-based drug delivery: a review of clinical studies," *Radioligand molecular imaging and biology: MIB: the official publication of the Academy of Radioligand molecular imaging*, vol. 20, pp. 683–695, 2018.
- [19] K. L. Moek, D. Giesen, I. C. Kok, D. J. A. de Groot, M. Jalving, and R. S. N. Fehrmann, "Theranostics using antibodies and antibody-related therapeutics," *Journal of Nuclear Medicine: Official Publication, Society of Nuclear Medicine*, vol. 58, pp. 83s–90s, 2017.
- [20] I. Verel, G. W. Visser, R. Boellaard, O. C. Boerman, J. van Eerd, and G. B. Snow, "Quantitative  $^{89}\text{Zr}$  immuno-PET for in vivo scouting of  $^{90}\text{Y}$ -labeled monoclonal antibodies in xenograft-bearing nude mice," *Journal of Nuclear Medicine: Official Publication, Society of Nuclear Medicine*, vol. 44, pp. 1663–1670, 2003.
- [21] M. V. Nestor, "Targeted radionuclide therapy in head and neck cancer," *Head & Neck*, vol. 32, pp. 666–678, 2010.
- [22] A. Wortmann, Y. He, E. Deryugina, J. Quigley, and J. Hooper, "The cell surface glycoprotein CDCP1 in cancer-insights, opportunities, and challenges," *IUBMB Life*, vol. 61, pp. 723–730, 2009.
- [23] T. Khan, T. Kryza, N. J. Lyons, Y. He, and J. D. Hooper, "The CDCP1 signaling hub: a target for cancer detection and therapeutic intervention," *Cancer Research*, vol. 81, pp. 2259–2269, 2021.
- [24] T. Kryza, T. Khan, S. Puttick, C. Li, K. A. Sokolowski, and B. W. Tse, "Effective targeting of intact and proteolysed CDCP1 for imaging and treatment of pancreatic ductal adenocarcinoma," *Theranostics*, vol. 10, pp. 4116–4133, 2020.
- [25] B. S. Harrington, Y. He, T. Khan, S. Puttick, P. J. Conroy, and T. Kryza, "Anti-CDCP1 immuno-conjugates for detection and inhibition of ovarian cancer," *Theranostics*, vol. 10, pp. 2095–2114, 2020.
- [26] C. T. Chou, Y. J. Li, C. C. Chang, C. N. Yang, P. S. Li, and Y. M. Jeng, "Prognostic significance of CDCP1 expression in colorectal cancer and effect of its inhibition on invasion and migration," *Annals of Surgical Oncology*, vol. 22, pp. 4335–4343, 2015.
- [27] A. Wortmann, Y. He, M. E. Christensen, M. Linn, J. W. Lumley, and P. M. Pollock, "Cellular settings mediating Src Substrate switching between focal adhesion kinase tyrosine 861 and CUB-domain-containing protein 1 (CDCP1) tyrosine 734," *Journal of Biological Chemistry*, vol. 286, pp. 42303–42315, 2011.
- [28] Y. He, C. M. Davies, B. S. Harrington, L. Hellmers, Y. Sheng, and A. Broomfield, "CDCP1 enhances Wnt signaling in colorectal cancer promoting nuclear localization of  $\beta$ -catenin and E-cadherin," *Oncogene*, vol. 39, pp. 219–233, 2020.
- [29] Y. He, A. C. Wu, B. S. Harrington, C. M. Davies, S. J. Wallace, and M. N. Adams, "Elevated CDCP1 predicts poor patient outcome and mediates ovarian clear cell carcinoma by promoting tumor spheroid formation, cell migration and chemoresistance," *Oncogene*, vol. 35, pp. 468–478, 2016.
- [30] B. M. Au - Zeglis and J. S. Au-Lewis, "The bioconjugation and radiosynthesis of  $^{89}\text{Zr}$ -DFO-labeled antibodies," *Journal of Visualized Experiments*, vol. 96, Article ID e52521, 2015.
- [31] J. Goos, M. Davydova, T. R. Dilling, A. Cho, M. A. Cornejo, and A. Gupta, "Design and preclinical evaluation of nanostars

- for the passive pretargeting of tumor tissue," *Nuclear Medicine and Biology*, vol. 84-85, pp. 63-72, 2020.
- [32] N. Percie du Sert, V. Hurst, A. Ahluwalia, S. Alam, M. T. Avey, and M. Baker, "The ARRIVE guidelines 2.0: updated guidelines for reporting animal research," *Experimental Physiology*, vol. 105, pp. 1459-1466, 2020.
- [33] E. I. Deryugina, E. M. Conn, A. Wortmann, J. J. Partridge, T. A. Kupriyanova, and V. C. Ardi, "Functional role of cell surface CUB domain-containing protein 1 in tumor cell dissemination," *Molecular Cancer Research*, vol. 7, pp. 1197-1211, 2009.
- [34] F. Bensch, M. M. Smeenk, S. C. van Es, J. R. de Jong, C. P. Schröder, and S. F. Oosting, "Comparative biodistribution analysis across four different (89)Zr-monooclonal antibody tracers-The first step towards an imaging warehouse," *Theranostics*, vol. 8, pp. 4295-4304, 2018.
- [35] Y. Vugmeyster, D. DeFranco, P. Szklut, Q. Wang, and X. Xu, "Biodistribution of [125I]-labeled therapeutic proteins: application in protein drug development beyond oncology," *Journal of Pharmaceutical Sciences*, vol. 99, pp. 1028-1045, 2010.
- [36] Y. Li, C. Jiang, X. Jiang, Z. Sun, M. M. Cona, and W. Liu, "Biliary and duodenal drainage for reducing the radiotoxic risk of antineoplastic 131I-hypericin in rat models," *Experimental Biology and Medicine*, vol. 240, pp. 1764-1773, 2015.
- [37] A. G. Arranja, V. Pathak, T. Lammers, and Y. Shi, "Tumor-targeted nanomedicines for cancer theranostics," *Pharmacological Research*, vol. 115, pp. 87-95, 2017.
- [38] V. J. Yao, S. D'Angelo, K. S. Butler, C. Theron, T. L. Smith, and S. Marchio, "Ligand-targeted theranostic nanomedicines against cancer," *Journal of Controlled Release: Official Journal of the Controlled Release Society*, vol. 240, pp. 267-286, 2016.
- [39] S. A. Graves, C. Kuttyreff, K. E. Barrett, R. Hernandez, P. A. Ellison, and S. Happel, "Evaluation of a chloride-based (89)Zr isolation strategy using a tributyl phosphate (TBP)-functionalized extraction resin," *Nuclear Medicine and Biology*, vol. 64-65, pp. 1-7, 2018.
- [40] T. K. Nayak and M. W. Brechbiel, "Radioimmunoimaging with longer-lived positron-emitting radionuclides: potentials and challenges," *Bioconjugate Chemistry*, vol. 20, pp. 825-841, 2009.
- [41] R. H. Stone, J. Hong, and H. Jeong, "Pharmacokinetics of monoclonal antibodies used for inflammatory bowel diseases in pregnant women," *Journal of Clinical Toxicology*, vol. 4, 2014.
- [42] K. Ogawa, K. Shiba, N. Akhter, M. Yoshimoto, K. Washiyama, and S. Kinuya, "Evaluation of radioiodinated vesamicol analogs for sigma receptor imaging in tumor and radionuclide receptor therapy," *Cancer Science*, vol. 100, pp. 2188-2192, 2009.
- [43] P. Wierstra, G. Sandker, E. Aarntzen, M. Gotthardt, G. Adema, and J. Bussink, "Tracers for non-invasive radionuclide imaging of immune checkpoint expression in cancer," *EJNMMI Radiopharmacy and Chemistry*, vol. 4, p. 29, 2019.
- [44] A. Natarajan, C. B. Patel, F. Habte, and S. S. Gambhir, "Dosimetry prediction for clinical translation of (64)Cu-pembrolizumab ImmunoPET targeting human PD-1 expression," *Scientific Reports*, vol. 8, p. 633, 2018.
- [45] H. Cai, J.-s Wu, O. Muzik, J.-T. Hsieh, R. J. Lee, and F. Peng, "Reduced <sup>64</sup>Cu uptake and tumor growth inhibition by knockdown of human copper transporter 1 in xenograft mouse model of prostate cancer," *Journal of Nuclear Medicine*, vol. 55, pp. 622-628, 2014.
- [46] H. Maeda, G. Y. Bharate, and J. Daruwalla, "Polymeric drugs for efficient tumor-targeted drug delivery based on EPR-effect," *European Journal of Pharmaceutics and Biopharmaceutics*, vol. 71, pp. 409-419, 2009.
- [47] Y. Shi, R. van der Meel, X. Chen, and T. Lammers, "The EPR effect and beyond: strategies to improve tumor targeting and cancer nanomedicine treatment efficacy," *Theranostics*, vol. 10, pp. 7921-7924, 2020.
- [48] F. C. van de Watering, M. Rijpkema, L. Perk, U. Brinkmann, W. J. Oyen, and O. C. Boerman, "Zirconium-89 labeled antibodies: a new tool for radioligand molecular imaging in cancer patients," *BioMed Research International*, vol. 2014, Article ID 203601, 12 pages, 2014.
- [49] C. Bailly, P. F. Clery, A. Faivre-Chauvet, M. Bourgeois, F. Guerard, and F. Haddad, "Immuno-PET for clinical theranostic approaches," *International Journal of Molecular Sciences*, vol. 18, 2016.
- [50] L. Y. Hu, K. A. Kelly, and J. L. Sutcliffe, "High-throughput approaches to the development of radioligand molecular imaging agents," *Radioligand Molecular Imaging and Biology: MIB: The Official Publication of the Academy of Radioligand Molecular Imaging*, vol. 19, pp. 163-182, 2017.
- [51] O. W. Press and J. Rasey, "Principles of radioimmunotherapy for hematologists and oncologists," *Seminars in Oncology*, vol. 27, pp. 62-73, 2000.
- [52] N. Zhao, Y. Qin, H. Liu, and Z. Cheng, "Tumor-targeting peptides: ligands for radioligand molecular imaging and therapy," *Anti-Cancer Agents in Medicinal Chemistry*, vol. 18, pp. 74-86, 2018.
- [53] IARC Monographs on the Evaluation of Carcinogenic Risks to Humans, "Ionizing radiation, part 2: some internally deposited radionuclides. views and expert opinions of an iarc working group on the evaluation of carcinogenic risks to humans. Lyon," *IARC Monographs on the Evaluation of Carcinogenic Risks to Humans*, vol. 78, pp. 1-559, 2001.
- [54] F. Paquet, G. Etherington, M. R. Bailey, R. W. Leggett, J. Lipsztein, and W. Bolch, "ICRP publication 130: occupational intakes of radionuclides: Part 1," *Annals of the ICRP*, vol. 44, pp. 5-188, 2015.